Detecting low-energy quasilocalized excitations in computer glasses

David Richard,[1,*] Geert Kapteijns,[2] and Edan Lerner[2]
[1]*Univ. Grenoble Alpes, CNRS, LIPhy, 38000 Grenoble, France*
[2]*Institute for Theoretical Physics, University of Amsterdam, Science Park 904, 1098 XH Amsterdam, The Netherlands*

(Received 3 April 2023; accepted 15 September 2023; published 11 October 2023)

Soft, quasilocalized excitations (QLEs) are known to generically emerge in a broad class of disordered solids and to govern many facets of the physics of glasses, from wave attenuation to plastic instabilities. In view of this key role of QLEs, shedding light upon several open questions in glass physics depends on the availability of computational tools that allow one to study QLEs' statistical mechanics. The latter is a formidable task since harmonic analyses are typically contaminated by hybridizations of QLEs with phononic excitations at low frequencies, obscuring a clear picture of QLEs' abundance, typical frequencies, and other important micromechanical properties. Here we present an efficient algorithm to detect the *field* of quasilocalized excitations in structural computer glasses. The algorithm introduced takes a computer-glass sample as input and outputs a library of QLEs embedded in that sample. We demonstrate the power of the algorithm by reporting the spectrum of glassy excitations in two-dimensional computer glasses featuring a huge range of mechanical stability, which is inaccessible using conventional harmonic analyses due to phonon hybridizations. Future applications are discussed.

DOI: 10.1103/PhysRevE.108.044124

I. INTRODUCTION

Understanding the manners in which amorphous solids deform when subjected to mechanical stresses is a long-standing challenge in condensed matter physics [1,2]. Key to achieving progress in solving this problem relies on the development of new, efficient computational tools that are able to characterize amorphous structures at the microscopic level—that are believed to govern glasses' mechanical response—in a useful manner [3]. Many numerical developments have been put forward in this context, including novel bond-order-parameters [4–6], machine-learning based tools [7–13], approaches based on the potential energy landscape (PEL) [14,15], and others [16–19].

Recently it has been shown that glassy defects generically take the form of soft quasilocalized excitations (QLEs) that are defined as displacement fields composed of a core of few tens of particles decorated by a long-range algebraic Eshelby-like decay [20]; see some visual representations in Fig. 1. QLEs assume the form of harmonic vibrations under certain conditions; in situations in which QLEs hybridize with phonons or other QLEs, they can be observed and their properties can be measured via the nonlinear excitations framework. In the low-frequency limit $\omega \to 0$, QLEs are known to abide by a universal nonphononic density of states $D(\omega) = A_g \omega^4$, where A_g has dimensions of $[\text{frequency}]^{-5}$ and controls the abundance of soft glassy defects in the system [20–27]. Soft QLEs control the magnitude of the nonaffine response that enters in calculation of the bulk shear modulus [28,29]. As such the depletion of excitations can reduce the fluctuations of shear moduli [30]. The latter is known to correlate well with the change in the attenuation rate of sound waves in structural glasses [30–32]. Finally, the abundance of soft QLEs has shown to correlate well with the toughness of different glass formers prepared with various cooling histories [33].

One of the main difficulties in studying these excitations within the harmonic approximation of the potential energy is that they hybridize with the overwhelming population of low-frequency phonons [34], present in any solid featuring a translationally invariant Hamiltonian. Due to said hybridizations, harmonic analyses do not allow one to systematically study QLE's individual dynamics, i.e., how a specific excitation will soften or stiffen upon mechanical loading [35], nor how QLEs interact with each other, i.e., how the softening or thermal activation of one excitation can affect the dynamics of remote excitations.

To circumvent the aforementioned hybridization issues, novel computational frameworks have been put forward, which offer various micromechanical definitions of soft QLEs [35–38] by incorporating anharmonic properties of the PEL. Within these nonlinear frameworks, a cost function associated with an arbitrary displacement field (referred to simply as a "mode") is constructed; these cost functions assume local minima at modes that simultaneously minimize the mode's energy, while maximizing its spatial localization. As demonstrated in [35,37,38], these frameworks allow one to filter out the phononic background from hybridized phonon-QLEs harmonic modes without having to modify particle interactions [39]. Furthermore, it has been demonstrated that the mechanics and spatial structure of quasilocalized excitations emerging from these nonlinear frameworks converge to those of harmonic excitations when hybridizations are absent

*david.richard@univ-grenoble-alpes.fr

[37,38], establishing the validity and usefulness of the nonlinear frameworks.

These nonlinear excitation frameworks were helpful in establishing several results and insights [38,40–42]. In the asymptotic low-frequency regime $\omega \to 0$, a link was found between the nonlinear mode frequency ω_π, the barrier height Δ, and the strain distance to a plastic instability x, as $\Delta \sim \omega_\pi^4$ and $x \sim \omega_\pi^3$, respectively [38]. This result was corroborated by investigating thermal activation in viscous liquids [43]. We thus expect soft QLEs to control short timescale thermal activations in viscous liquids [44] and imminent plastic instabilities in driven solids [3,14,15]. Moreover, it was recently demonstrated that harmonic excitations present in the Boson peak as excess modes from the Debye theory can be reconstructed from a linear combination of stiff QLEs [42]. Yet an exhaustive detection and extraction of the entire population of QLEs from a given computer-glass sample is still missing.

In this work we address this issue and present an algorithm that builds on the same aforementioned nonlinear excitation frameworks; it takes as input a computer-glass sample and outputs a library of the (nonlinear) QLEs embedded in that glass. We demonstrate the usefulness of our algorithm by applying it to study the effect of thermal annealing on the abundance of QLEs in model glasses, and discuss further research directions that the algorithm may open up.

This paper is structured as follows; we first provide the reader with a brief theoretical background of the nonlinear excitations framework, followed by a detailed presentation of our developed QLE-detection tools in Sec. II. In Sec. III we investigate the impact of some of the input parameters of our algorithm and of the choice of the particular nonlinear cost function employed on the extracted nonphononic spectrum of a model glass, and compare it directly with the harmonic vibrational density of states (vDOS) in three-dimensional (3D) systems. In Sec. IV we employ the presented algorithm to examine the effect of thermal annealing on the statistics of QLEs in both two-dimensional (2D) and 3D computer glasses. Finally, in Sec. V we discuss the perspectives of our algorithm to study viscous dynamics of supercooled liquids, in addition to the mechanical response of amorphous solids.

II. THEORETICAL AND NUMERICAL FRAMEWORK

In this section, we spell out an important theoretical background, which forms the basis of our QLE-detection algorithm. We also describe key features and caveats of our detection algorithm.

A. Cost functions

We consider a system composed of N particles in d spatial dimensions with volume V, number density $\rho = N/V$, and shear modulus μ. As shown in Ref. [20] and visualized in Fig. 1, soft spots in a glass can be realized as Nd-dimensional displacement fields $\boldsymbol{z}$ that are composed of a localized core of a few tens of particles, decorated by a long-range field that decays as $r^{-(d-1)}$ at distance r away from the core. Various nonlinear frameworks introduced [35–38] that enable the extraction of such excitations are all based on finding displacement fields $\boldsymbol{\pi}$ at which a high-dimensional cost function

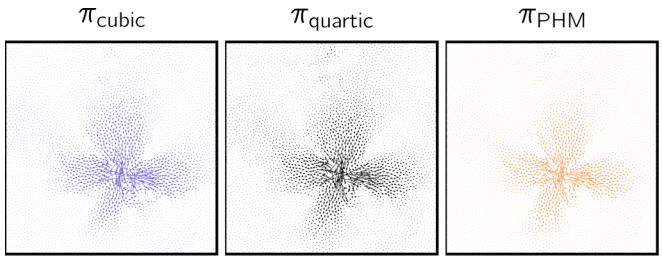

FIG. 1. Different realizations of the same nonlinear mode extracted from the cubic (a), quartic (b), and PHM (c) cost function. Mode energies are $\kappa_{\text{cubic}} = 0.428$, $\kappa_{\text{quartic}} = 0.347$, and $\kappa_{\text{PHM}} = 0.357$, respectively.

$\mathcal{C}(\boldsymbol{z})$ assumes local minima:

$$\left.\frac{\partial \mathcal{C}}{\partial \boldsymbol{z}}\right|_{\boldsymbol{z}=\boldsymbol{\pi}} = \boldsymbol{0}. \tag{1}$$

Here $\mathcal{C}(\boldsymbol{z})$ is constructed in order to penalize both high-energy *and* delocalized (spatially extended) displacement fields. As such, plane waves—which are inherently present in the harmonic approximation of any solid and are generically spatially extended—are suppressed and do not form solutions to Eq. (1). As presented in detail in Refs. [35–38], there are different ways to construct cost functions $\mathcal{C}(\boldsymbol{z})$ that can be practical [35] and/or physically motivated [36]. We next review the three cost functions ones used throughout this work, namely, the cubic [36], quartic [37], and pseudoharmonic cost functions [35], distinguished in our notation by the subscript of $\mathcal{C}(\boldsymbol{z})$.

In the cubic cost-function framework, $\mathcal{C}_{\text{cubic}}(\boldsymbol{z})$ is the "barrier function" that follows from a third-order expansion of the energy with respect to displacements; it reads

$$\mathcal{C}_{\text{cubic}}(\boldsymbol{z}) = \frac{\kappa^3}{\tau^2}, \tag{2}$$

where $\kappa(\boldsymbol{z}) \equiv \boldsymbol{\mathcal{H}} : \boldsymbol{zz}$ is the mode energy, and $\tau(\boldsymbol{z}) \equiv \boldsymbol{\mathcal{T}} : \cdot\, \boldsymbol{zzz}$ is the mode asymmetry, where $\boldsymbol{\mathcal{T}} \equiv \partial^3 U/\partial \boldsymbol{x}\partial \boldsymbol{x}\partial \boldsymbol{x}$ is the tensor of third-order derivatives of the energy with respect to particle coordinates. Here and in what follows, single, double, triple, and quadruple contractions over Cartesian components and particle indices are denoted by $\cdot$, $:$, $: \cdot$, and $::$, respectively.

The quartic cost function follows from an analogy with $\mathcal{C}_{\text{cubic}}$; here the third-order contraction τ is replaced with the fourth-order contraction $\chi(\boldsymbol{z}) \equiv \boldsymbol{\mathcal{M}} :: \boldsymbol{zzzz}$, where $\boldsymbol{\mathcal{M}} = \partial^4 U/\partial \boldsymbol{x}\partial \boldsymbol{x}\partial \boldsymbol{x}\partial \boldsymbol{x}$ is the fourth-order derivative of the energy with respect to particle coordinates, giving [37]

$$\mathcal{C}_{\text{quartic}}(\boldsymbol{z}) = \frac{\kappa^4}{\chi^2}. \tag{3}$$

We note that χ has been shown to be inversely proportional to the mode participation ratio $e \equiv [N \sum_i (\boldsymbol{z}_i \cdot \boldsymbol{z}_i)^2]^{-1}$ [37], hence the denominator of $\mathcal{C}_{\text{quartic}}$ will promote localization upon minimization.

It is typically cumbersome to compute the contractions τ and χ in systems employing many body interactions, or even ill-defined in cases that the employed interaction potentials are not smooth enough, e.g., Hertzian spheres. To overcome these difficulties, we have recently introduced a framework

for extracting QLEs that solely utilizes the harmonic approximation of the potential energy [35]. The excitations that emerged from this framework were coined pseudoharmonic modes (PHMs) since they require access only to the harmonic approximation of the energy. The associated cost function reads

$$\mathcal{C}_{\rm PHM}(\boldsymbol{z}) = \frac{\kappa^2}{\sum_{\langle i,\, j\rangle}(\boldsymbol{z}_{ij}\cdot\boldsymbol{z}_{ij})^2}, \tag{4}$$

where i, j are particle indices, $\boldsymbol{z}_{ij} \equiv \boldsymbol{z}_j - \boldsymbol{z}_i$, and the sum in Eq. (4) runs over all pairs $\langle i, j\rangle$ of interacting particles. For systems with long-ranged interactions, one can run the sum over close neighbors defined, e.g., by a Voronoi analysis. Spatially extended, low-frequency plane waves have inherently small displacement gradients, i.e., small local $\boldsymbol{z}_{ij}$, and thus increase the cost function in favor of QLEs with larger $\boldsymbol{z}_{ij}$ components at the mode's core.

In Fig. 1 we show the same realization of a soft mode as a solution of Eq. (1) for the three different cost functions $\mathcal{C}_{\rm cubic}(\boldsymbol{z})$, $\mathcal{C}_{\rm quartic}(\boldsymbol{z})$, and $\mathcal{C}_{\rm PHM}(\boldsymbol{z})$ described above. As already discussed more quantitatively in Ref. [38], we find a similar mode geometry with a nearly perfect mode overlap: $\boldsymbol{\pi}_{\rm cubic}\cdot\boldsymbol{\pi}_{\rm quartic} \simeq 0.974$, $\boldsymbol{\pi}_{\rm cubic}\cdot\boldsymbol{\pi}_{\rm PHM} \simeq 0.965$, and $\boldsymbol{\pi}_{\rm quartic}\cdot\boldsymbol{\pi}_{\rm PHM} \simeq 0.999$. Note that subtle but important differences exist between cubic and quartic/PHM modes as the former includes anharmonic information about the potential energy landscape. As a result, cubic modes provide a better estimation (compared to the other considered cost functions) of configuration-space directions that tend to move the system across saddle points, at the cost of a slightly higher mode energy [38]. This point is further discussed in Sec. III. A more detailed comparison between the properties of nonlinear modes extracted from the different cost functions can be found in Refs. [35,37,38].

B. Mapping dipole forces

Since the aforementioned cost functions are nonlinear, finding local minima of these function requires one to provide an initial guess—denoted in what follows as $\boldsymbol{z}_0$—for the minimization of the employed cost function; see Ref. [36] for a visual demonstration. Our algorithm is constructed to provide spatially distinct initial guesses $\boldsymbol{z}_0$ in order to efficiently and exhaustively find local minima of the employed cost function $\mathcal{C}$.

To this aim, we first harvest local force dipoles, as illustrated in Fig. 2. We uniformly divide our system to blocks of linear size ξ; the latter is chosen to be consistent with the typical core size of QLEs (usually between 5 and 10 particle diameters [25]). Next, we consider the responses to local force dipoles $\boldsymbol{f}$ acting on a pair of particles $\{ij\}$ centered in each block; see Fig. 2. These local force dipoles constitute excellent initial conditions $\boldsymbol{z}_0$ for finding modes $\boldsymbol{\pi}$ that are also located at the center of each cell (if such a mode exists); see example in Fig. 2. In parallel, we have harvested the displacement response $\boldsymbol{u}$ to the same force dipole as obtained by solving the the linear equation $\mathcal{H}\cdot\boldsymbol{u} = \boldsymbol{f}$. As shown in Ref. [45], displacements $\boldsymbol{u}$ will be dominated by soft modes present in $\mathcal{H}$ that project well onto the force $\boldsymbol{f}$ and thus serve as potential initial guesses to find minima of $\mathcal{C}$. We have found

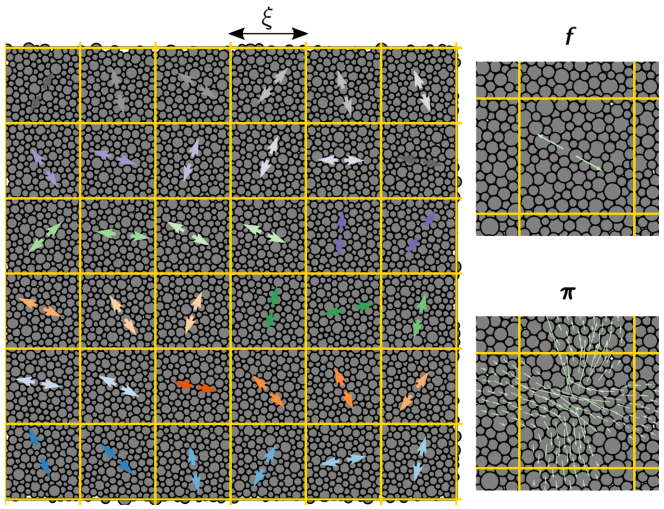

FIG. 2. Sketch of *stage 1* of our algorithm: (1) we probe glassy heterogeneities on a scale ξ, (2) we pinch two particles with a force $\boldsymbol{f}$ at the center of each block (here rendered with different colors), and (3) we map $\boldsymbol{f}$ onto a solution $\boldsymbol{\pi}$ of a given nonlinear cost function $\mathcal{C}$.

similar results by directly starting our minimization from $\boldsymbol{f}$, thus avoiding the extra cost of solving the aforementioned linear equation, and by such substantially reducing the computational complexity of our algorithm.

At this point, we have specified *stage 1* of our algorithm, namely:

(1) Partition the system into blocks of linear size ξ.

(2) Pinch a pair of particle with a force $\boldsymbol{f}$ in the center of each block.

(3) Map the dipole force $\boldsymbol{f}$ onto a mode $\boldsymbol{\pi}$.

C. The "halo" effect

In Fig. 3 we present an example in which the first part of our QLE-detection algorithm described above is applied to two glass samples prepared by the SWAP Monte Carlo (MC) scheme [46], which enables one to equilibrate liquids down to very low temperatures, i.e., at very strong supercooling. Those equilibrium configurations are then instantaneously quenched to zero temperature to form an ensemble of glasses labeled by the equilibrium parent temperature $T_{\rm p}$. With this scheme, we are able to build ensembles of glass samples featuring a very wide range of mechanical stability. The model's details and units employed can be found in Appendix A. Here we have considered two extreme cases of a very stable, "cold" glass [Fig. 3(a)] and a poorly annealed "hot" glass [Fig. 3(b)] prepared at $T_{\rm p} = 0.2$ and $T_{\rm p} = 0.7$, respectively.

Our main goal is to probe homogeneously excitations on a scale ξ without redundancies, as well as with a minimum amount of mapping procedures as the latter constitutes the computational bottleneck of our method. For the stable, low-$T_{\rm p}$ glass, this goal is achieved where each mapping from a dipole force leads to a *distinct* solution $\boldsymbol{\pi}$ associated with a frequency $\omega_\pi \equiv \sqrt{\mathcal{H}:\boldsymbol{\pi}\boldsymbol{\pi}}$. In contrast, we find in our poorly annealed sample that many dipole forces $\boldsymbol{f}$ map (under the minimization of the $\mathcal{C}_{\rm PHM}$ cost function) to the *same* solution $\boldsymbol{\pi}$, resulting in "empty" regions in the glass where there are

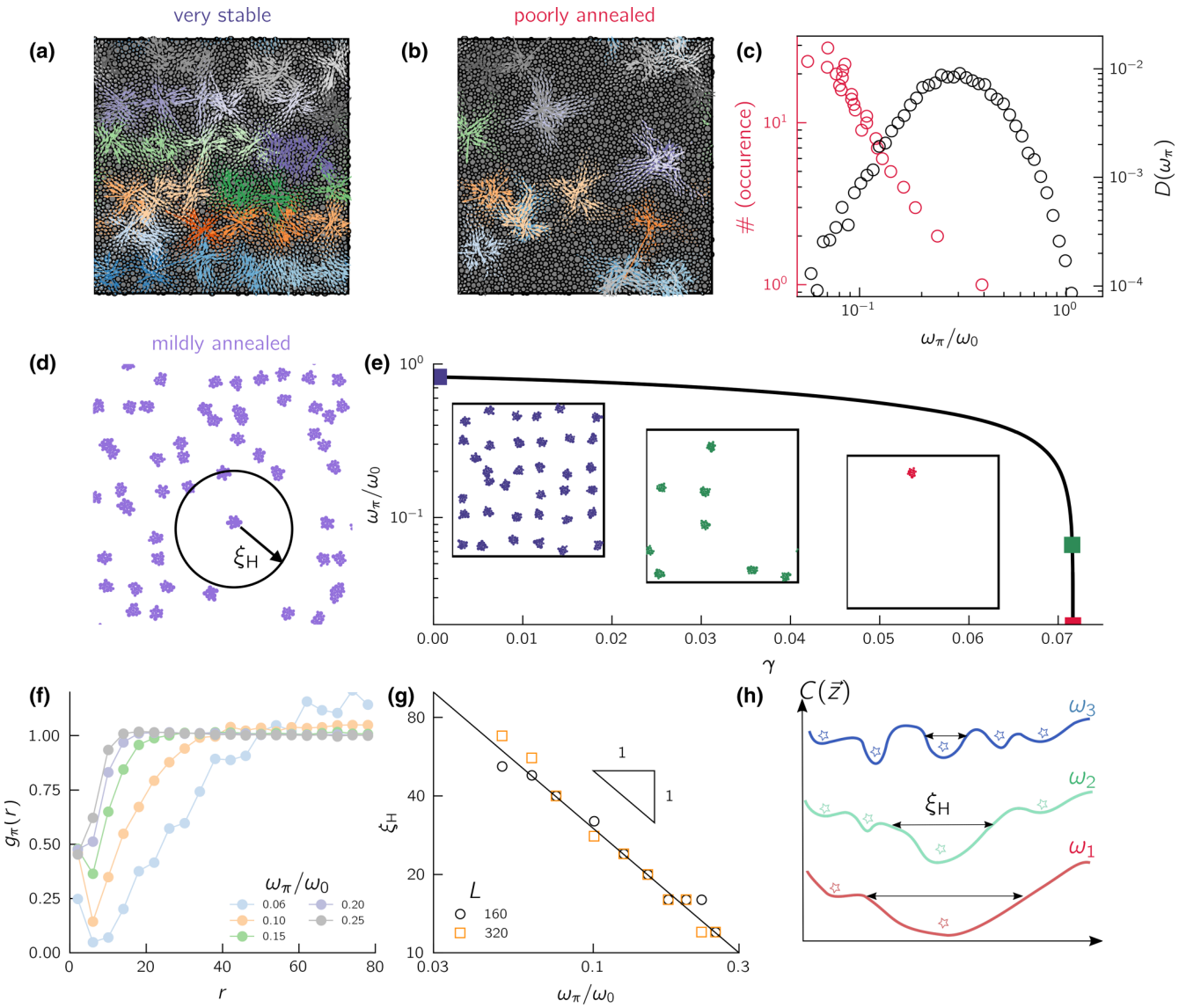

FIG. 3. First stage of our detection algorithm applied on a very stable (a) and poorly annealed (b) glass prepared at $T_p = 0.2$ and 0.7, respectively. Different colors correspond to different dipole forces used to start the mapping procedure, such as shown in Fig. 2. (c) Occurrence number (red) and density of states (black) as a function of the mode frequency ω for a glass prepared at $T_p = 0.7$. (d) Example of the halo effect in a large mildly annealed glass composed of $N = 102\,400$. (e) Example of the halo effect when approaching a plastic instability. The black curve is the mode frequency as a function of the strain. Insets show our algorithm at different strains marked by colored squares. (f) Mode radial distribution function $g_\pi(r)$ for different mode π with frequency ω_π. (g) Halo radius ξ_H as a function of ω_π for two different box lengths L. $\omega_0 \equiv c_s/a_0$ with c_s and a_0 denoting the shear-wave speed $c_s = \sqrt{\mu/\rho}$ and typical interparticle distance, respectively. The black line indicates the scaling $\xi_H \sim 1/\omega_\pi$. (h) Sketch of the cost function landscape $\mathcal{C}(z)$ approaching the limit $\omega_\pi \to 0$ as illustrated in (e). Different colors correspond to different frequencies ω_π of one soft excitation with $\omega_1 < \omega_2 < \omega_3$. Each star represents a distinct solution associated to one minimum of $\mathcal{C}(z)$. The size of the halo created by the lowest excitation is indicated by horizontal double arrows. All modes are extracted using $\mathcal{C}_{\text{PHM}}$.

presumably no QLEs. This effect, referred to as the "halo effect" in what follows, is driven by the thermal-history induced changes in the properties of the cost functions $\mathcal{C}(z)$ and is quantified in Fig. 3(c), where we compare the (re-)occurrence number of modes versus their frequency ω_π with the density of states $D(\omega_\pi)$. Here we have used an ensemble of 200 independent samples with $N = 4096$ particles prepared at $T_p = 0.7$. Here and in what follows, density of states is normalized by $N \times d \times N_s$, with N_s the number of independent samples. Note that the same normalization is applied on the nonlinear spectrum of QLEs. Interestingly, we find that the lower the frequency, the higher the chance that a minimizations starting from dipole force $\boldsymbol{f}$ located away from the mode's core will be mapped to the exact same mode. In other words, the direction-space *volume* of the basins of the cost function $\mathcal{C}(z)$—that correspond to very low-frequency modes—increases with decreasing mode frequency. Indeed, since the spectrum of quasilocalized excitations is gapless [41], we expect that a similar halo effect will be at play for glasses of any stability (i.e., including very stable glasses), in

the large system size limit $N \to \infty$. To illustrate this point we prepare a large mildly annealed 50-50 binary mixtures with $N = 102\,400$ equilibrated by conventional molecular dynamics [47], and show in Fig. 3(d) a close-up on one specific soft mode that reveals an approximated circular halo of radius ξ_H, in which no other solution of $\mathcal{C}_{\rm PHM}$ are found.

We also expect the emergence of the halo effect in mechanically driven solids, as the frequency of destabilizing modes on the brink of plastic instabilities can be arbitrary low, potentially giving rise to a large halo effect. This second situation is illustrated in Fig. 3(e), where we plot the frequency ω_π of a destabilizing mode as a function of the strain γ upon a simple shear deformation. The insets of Fig. 3(e) show the catalog of modes at different strain distance [indicated by colored squares in $\omega_\pi = f(\gamma)$] to a mechanical (plastic) instability. At the onset of the plastic instability, $\mathcal{C}_{\rm PHM}$ exhibits only one minimum, which corresponds to the critical mode (shown as a red blob of particles).

Next we want to quantitatively measure the relation between ξ_H and the frequency ω_π of the underlying soft mode. Here we compute the averaged radial distribution function $g_\pi(r)$ between a mode of frequency ω_π and all other solutions found with our algorithm; see Fig. 3(f). $g_\pi(r)$ is normalized by the ideal gas distribution, with the number density computed from the total number of *different* solutions $\boldsymbol{\pi}$ found for a given glass realization. At large distances, g_π goes to unity indicating that QLEs are randomly distributed with a uniform density. At small distances, we observe a gap that grows as ω_π decreases. We extract an estimate for ξ_H at which $g_\pi(r) > 0.9$ and plot it in Fig. 3(g) against ω_π. We find that the two are inversely related, namely, $\xi_H \sim \omega_\pi^{-1}$, confirming that in the low-frequency limit the halo effect will be system spanning. In Fig. 3(h) we sketch how the landscape of $\mathcal{C}$ changes in the limit $\omega_\pi \to 0$. The size ξ_H of the metabasin diverges until $\mathcal{C}$ exhibits progressively only a single minimum. The same behavior is observed for all three cost functions $\mathcal{C}(z)$ described in Sec. II. Together, we can expect the "halo" effect to always be at play in the thermodynamic limit, independent of glass stability. However, for finite systems, as the population of low-frequency QLEs decreases drastically with cooling, the volume of basins associated with minima of the cost function $\mathcal{C}$ will remain small, as illustrated by the blue example ($\omega_\pi = \omega_3$) in Fig. 3(h).

D. Biasing procedure

To circumvent the halo effect described in the previous subsection—namely, to find QLEs in regions of the glass that seem "empty"—we propose to bias the employed cost function by systematically and artificially stiffening modes. In practice, this is done by connecting by a Hookean spring with stiffness κ_b two particles residing at the center of the to-be-stiffened soft mode. In order to avoid overstiffening the system, we choose κ_b to be equal to the median of the interaction stiffness distribution. As a natural choice, we choose to stiffen the pair $\{ij\}$ corresponding to the largest relative longitudinal displacement between particles. The procedure is spelled out as follows; after mapping the force $\boldsymbol{f}$ onto a mode $\boldsymbol{\pi}$, we check whether or not this mode resides within its box of size ξ. If the resulting mode $\boldsymbol{\pi}$ does not reside in the box

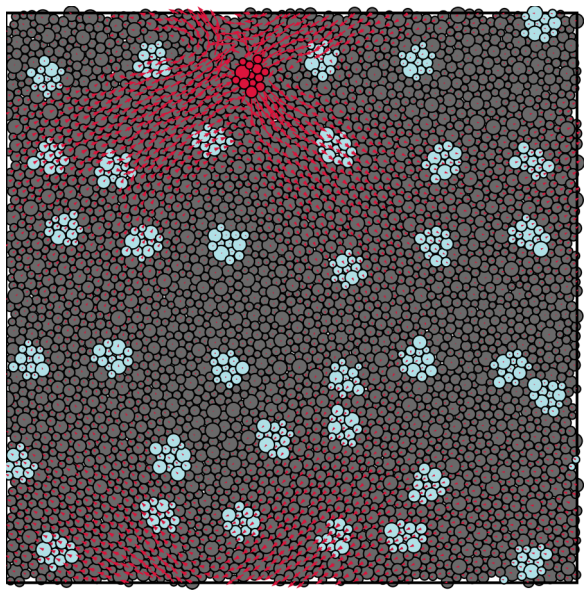

FIG. 4. Example of our detection algorithm on a glassy configuration at the onset of a plastic instability with critical mode $\boldsymbol{\pi}_c$ ($\omega_{\pi_c}/\omega_0 \simeq 0.02$) rendered in red. Each blob of particles colored in cyan corresponds to the core of a distinct mode.

associated with $\boldsymbol{f}$, we add a Hookean spring to the core of $\boldsymbol{\pi}$ and repeat the mapping of $\boldsymbol{f}$ until a successful detection of a mode *within* the box is made.

As an extreme test case, we quasistatically shear a stable glass sample up to the first encountered plastic instability (up to strain $\gamma_c \simeq 0.07$), as previously shown in Fig. 3(e). Recall that, upon approaching γ_c, we find that *all* dipole forces $\boldsymbol{f}$ are mapped onto a single mode $\boldsymbol{\pi}$—the destabilizing mode $\boldsymbol{\pi}_c$—rendered in red in Fig. 4. We now apply our biasing procedure and connect a Hookean spring of stiffness κ_b between a pair of particles at the core of $\boldsymbol{\pi}_c$. Repeating stage 1 of the algorithm, we are able to recover excitations in the entire system, including ones in close spatial proximity to $\boldsymbol{\pi}_c$. We note, importantly, that each mode's frequency $\omega_\pi \equiv \sqrt{\boldsymbol{\mathcal{H}} : \boldsymbol{\pi}\boldsymbol{\pi}}$ is computed after removing all biasing (stiffening) springs.

We have now completed the description of stage 2 of our QLE-detection algorithm, namely:

(4) If a mapping of $\boldsymbol{f}$ results in a mode $\boldsymbol{\pi}$ residing *outside* the block associated with $\boldsymbol{f}$, we stiffen it with a spring of stiffness κ_b.

(5) Repeat step 4 until the detected mode $\boldsymbol{\pi}$ resides within the block associated with $\boldsymbol{f}$.

Combining stages 1 and 2 of the algorithm allows the extraction of the entire library of QLEs of a glass sample. The algorithm time $t_{\rm algo}$ needed to build a catalog for a fixed ξ scales as $N^{2.4}$, as shown in Appendix B. The scaling is explain by (1) the linear extensive nature of the catalog size for a fixed ξ, (2) the extra linear complexity with N of solving linear equations for a given mode $\boldsymbol{\pi}$, and (3) that the "halo" effect is more pronounced in larger systems, hence one needs to repeat step 4 more often. Importantly, we note that the QLE catalog obtained with our algorithm does not depend on the sequence of blocks inspected and therefore can be trivially parallelized to investigate large system sizes.

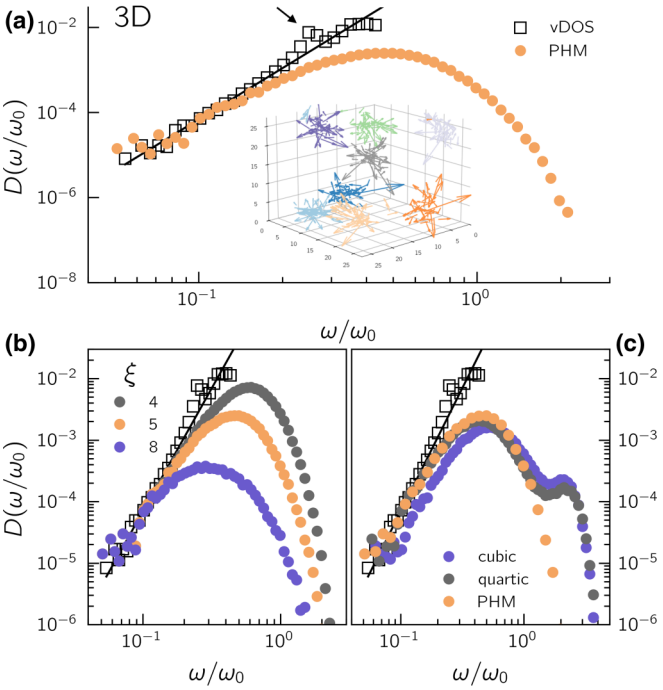

FIG. 5. (a) Comparison between the harmonic and PHM vDOS in mildly annealed 3D glasses composed of $N = 2000$ with $\xi = 5$. The arrow indicates the first shear wave. The inset shows eight modes detected in a sample composed of $N = 16\,000$ with $\xi = 10$. (b) Effect of partitioning length ξ on the PHM spectrum. (c) PHM spectrum for different cost function with $\xi = 5$. The system is a 3D polydisperse glass prepared at $T_p = 0.6$.

III. VALIDATION OF THE ALGORITHM

As a validation benchmark, we directly compare the harmonic vDOS of computer glasses with the spectrum of pseudoharmonic modes (PHMs) extracted using the QLE-detection algorithm spelled out above. Without compromising generality, we perform this comparison using mildly annealed 3D glasses with $N = 2000$ particles (see Appendix A for details). The motivation for this choice is to consider computer glasses featuring a relatively high abundance of QLEs that can be easily measured using a conventional harmonic spectral analysis.

In Fig. 5(a) we report the PHM spectrum for the partitioning length $\xi = 5$ (expressed in terms of the typical interparticle distance a_0). The inset shows eight modes extracted using our algorithm in a 3D sample. We find a good agreement between the harmonic and PHM vDOS below the first phonon (indicated by a small arrow): We find a gapless distribution at low frequencies that displays the same $\sim\omega^4$ scaling as seen for the harmonic modes vDOS. At higher frequencies, the PHM vDOS exhibits a maximum before decreasing and vanish at a characteristic upper cutoff frequency.

We next vary ξ from four to eight; see Fig. 5(b). In a system of $N = 2000$ this corresponds to extracting between one and eight modes per sample. For $\xi = 8$, we already recover a large fraction of nonlinear modes that populate the low-frequency tail of the harmonic vDOS. As ξ decreases, we progressively pick up stiffer modes that extend well above the first shear wave. Decreasing further ξ will thus result in the detection of high-frequency excitations. To illustrate this point, we present in Fig. 6 a 2D example that display the location of PHM excitations for a different level of coarse graining with ξ ranging from 5 to 20. We render PHMs that populate the quartic regime ($\omega_\pi/\omega_0 < 0.2$) and stiffer nonlinear modes as red displacement fields and cyan blobs, respectively. The majority of excitations populating the quartic regime are recovered with $\xi \simeq 10$–20. Moreover, we find the spatial location of the softest excitations to be the same for different ξ.

Finally, we set $\xi = 5$ and investigate the nonphononic spectrum obtained using different cost functions. In Fig. 5(c) we compare results obtained using the PHM-cost function with those obtained using the cubic and quartic cost functions, detailed in Sec. II. At low frequencies we find that PHMs and quartic modes have the lowest energy and produce the same low-frequency tail as the conventional harmonic vDOS.

In contrast, the excitations obtained using the cubic cost function (referred to as *cubic modes*) are found to be slightly stiffer (as also pointed out in Ref. [37]). This slightly higher energy of cubic modes is explained by the need of maximizing the mode asymmetry when minimizing $\mathcal{C}_{\text{cubic}}$. However, cubic modes still exhibit the correct quartic scaling $D(\omega) \sim \omega^4$.

At high frequencies, we find for the cubic and quartic modes a second peak in their respective spectra. The same double-peak distribution is observed in 2D glasses, as shown in Appendix C. Inspecting modes populating the first and second peak, we find that stiff modes show a less quadrupolar anisotropy compared with their low-frequency counterpart; see Fig. 7. We link this second population to the presence of large pairwise forces that increases the denominator of $\mathcal{C}_{\text{cubic}}$ and $\mathcal{C}_{\text{quartic}}$, the force magnitude being absent in $\mathcal{C}_{\text{PHM}}$. The resulting mode geometry corresponds to two particles being pushed away from each other. We note that a similar behavior of the excitation distribution was observed when investigating the statistical mechanics of dipole responses [45].

IV. APPLICATIONS

A. Nonphononic spectrum of 2D structural glasses

Recently it has been debated whether or not 2D computer solids feature the same $\sim\omega^4$ scaling of their nonphononic vDOS as 3D solids do [48–52]. One of the difficulties to investigate the QLE statistics in two dimensions is that one needs to employ large enough samples to avoid finite-size effects [51,53], typically of a few thousand of particles in size. The lateral box length L for such system sizes is typically on the order 50–100 particle diameters. The frequency of the first shear wave decreases as $\omega_{\text{ph}} \sim L^{-1}$, and the onset of QLEs scales as $\sim L^{-2/5}$ [21]. As a consequence, most of the QLEs that populate the low-frequency, harmonic nonphononic spectrum are hybridized with plane waves. More details can be found in Ref. [34]. This limiting issue is even more pronounced for very stable glasses, since in those systems the population of QLEs is both stiffened and depleted [25,40,45]. So far, due to the aforementioned difficulties and in contrast to 3D solids, there have been no reports on how the nonphononic prefactor A_g varies as a function of the parent temperature T_p in two dimensions. Below we show that our QLE-detection algorithm is able to provide this information.

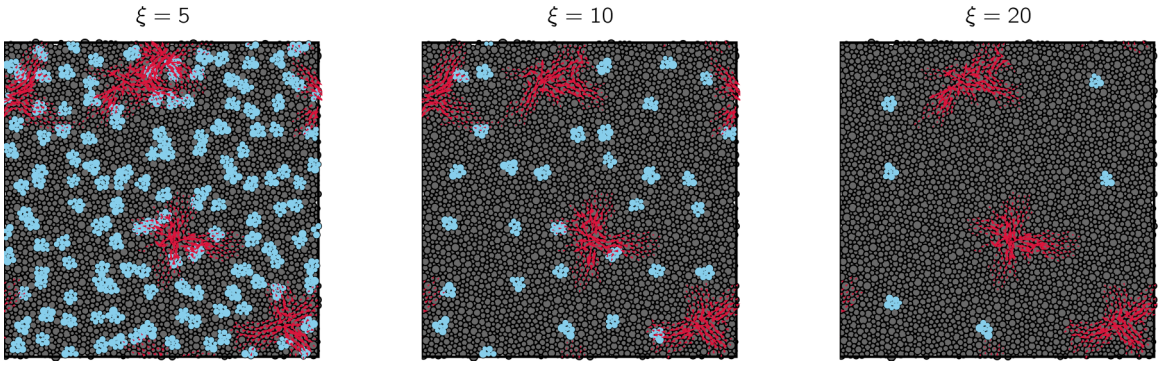

FIG. 6. Location of PHM excitations extracted from our biasing algorithm with different coarse-graining length ξ. PHMs that populate the quartic scaling ($\omega_\pi/\omega_0 < 0.2$) are rendered as red displacement fields. Stiffer excitations are rendered as cyan blobs.

Additionally, due to the QLE-detection algorithm we are now able to also identify the upper frequency limit up to which QLEs exist and observe its variability with changing glass stability. Our results are shown in Fig. 8; in Fig. 8(a) we compare the 2D harmonic vDOS with the PHM spectrum of a poorly annealed ($T_p = 1.0$) and very stable ($T_p = 0.2$) glasses (see Appendix A for details about the model and its units). We observe a strong suppression of the prefactor of ω^4 tail as well as a shift of the QLM spectrum towards larger frequencies.

In Fig. 8(b) we show the complete PHM spectrum rescaled by ω^4 for various T_p. We find a plateau at low frequency confirming that the nonphononic statistics in two dimensions follows $D(\omega) = A_g\omega^4$ for $\omega \to 0$. We note that small deviations from the ω^4 scaling are observed for hyperquenched glasses ($T_p > 0.5$), fully consistent with the known finite-size effects [51,53]. We show in Appendix D that we recover the scaling ω^4 for $N = 102\,400$. In addition, one can read the values of A_g off the $\omega \to 0$ plateau values of $D(\omega)/\omega^4$; we find a similar variability of A_g compared to 3D observations [25,54]—of over three decades—with a drop of about three orders of magnitude when decreasing T_p.

Collecting from our catalog the lowest mode in each glassy configuration, we can compute the average of the square of the mode amplitude decay $|\pi|^2$ that populate the ω^4 scaling. As shown in Ref. [25], one can rescale $|\pi|^2$ by its algebraic decay, $\sim r^{-2}$, and extract an estimate for the typical core size ξ_π at which $r^2|\pi|^2$ shows a maximum; see Fig. 8(c). We clearly observe a decrease of ξ_π for very stable glasses. This result is in line with previous numerical studies for 3D amorphous solids [25,54].

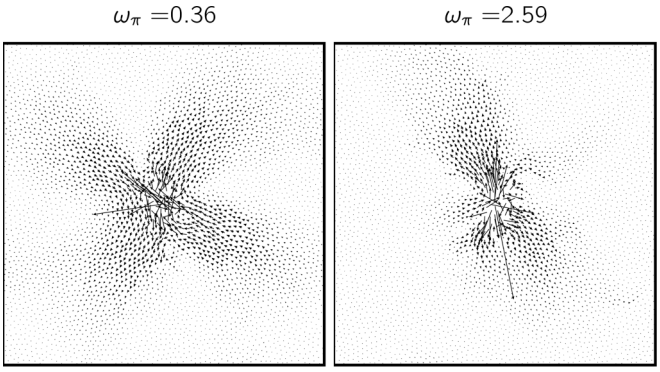

FIG. 7. Low- (left) and high-frequency (right) cubic modes extracted in a mildly annealed 2D polydisperse glass prepared at $T_p = 0.6$. Modes have been shifted to the center of the simulation box for the sake of visibility.

B. Robustness and caveats

We now discuss the robustness and caveats of our algorithm in regard to the extraction of A_g and ω_π as a function of T_p. As already pointed out in Fig. 5(b), decreasing ξ results in the detection of stiffer modes. In Fig. 9(a) we show the 2D PHM spectra for $\xi = 5$ and $\xi = 10$ measured in glassy samples ranging from poorly annealed ($T_p = 1.0$) to very stable ($T_p = 0.2$). As observed in 3D glasses the low-frequency spectrum is unchanged upon decreasing ξ. As a consequence, the range of A_g vs T_p does not vary with ξ, as shown in Fig. 9(b).

For stable glasses, we also observe that the typical frequency scale $\langle\omega_\pi\rangle$ remains constant under variations of ξ. This is not the case for poorly annealed samples, where $\langle\omega_\pi\rangle$ slowly increases with decreasing ξ; see arrows in Fig. 9(a). As a result, the relative stiffening of $\langle\omega_\pi\rangle/\langle\omega_\infty\rangle$ with thermal annealing decreases with ξ; see Fig. 9(c). Interestingly, we find that when ξ approaches the typical QLM core size ξ_π (about three to five particle diameters), $\langle\omega_\pi\rangle/\langle\omega_\infty\rangle$ exhibits the same range as previously found when extracting an energy scale from the dipole response statistics [45]. We have found similar results in our 3D glassy solids.

C. Effect of thermal 2D vs 3D annealing

In what follows, we define the typical mode frequency $\langle\omega_\pi\rangle$ as the *average* frequency of the full QLE spectrum. We are now in position to extract both the abundance of soft excitations through the dimensionless prefactor A_g, the characteristic mode frequency $\langle\omega_\pi\rangle$, and the core size ξ_π. Additional data for 3D glasses are provided in Appendix E. Here we propose a comparison of 2D and 3D solids as a function of glass stability controlled by T_p. Note that this direct comparison is meaningful as both our 2D and 3D systems share the same onset temperature $T_{onset} \simeq 0.6$.

In Fig. 10(a) we plot A_g as a function of T_p normalized by the high-temperature plateau value A_∞. As discussed

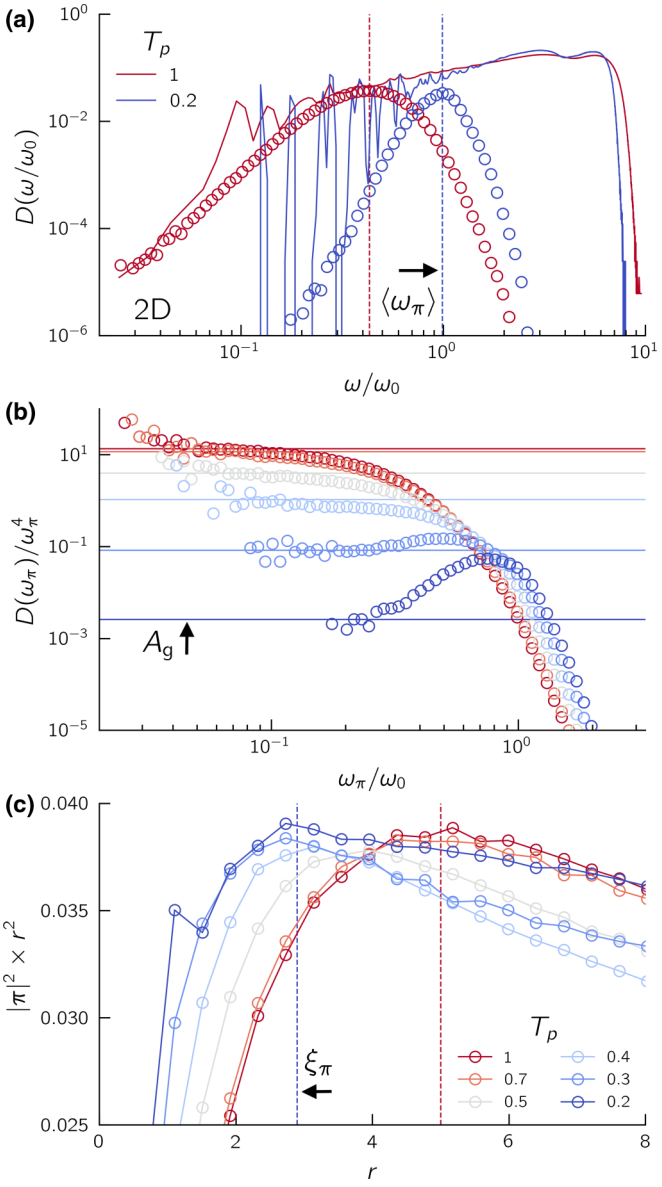

FIG. 8. (a) Comparison between the full harmonic (solid lines) and PHM (empty circles) vDOS for 2D glasses with $N = 4096$ quenched from parent temperatures T_p as indicated by the legend. PHM spectra are computed using $\xi = 5$. The dashed vertical lines indicate the shift of the *average* mode frequency ω_π between our most stable glassy configurations (blue) and hyperquenched glasses (red). (b) Rescaled PHM vDOS for various parent temperature T_p with $\xi = 5$. The horizontal lines indicate A_g. (c) Rescaled square of the mode amplitude decay $|\pi|^2$ by r^2. Vertical dashed lines indicate the reduced core size ξ_π when decreasing T_p.

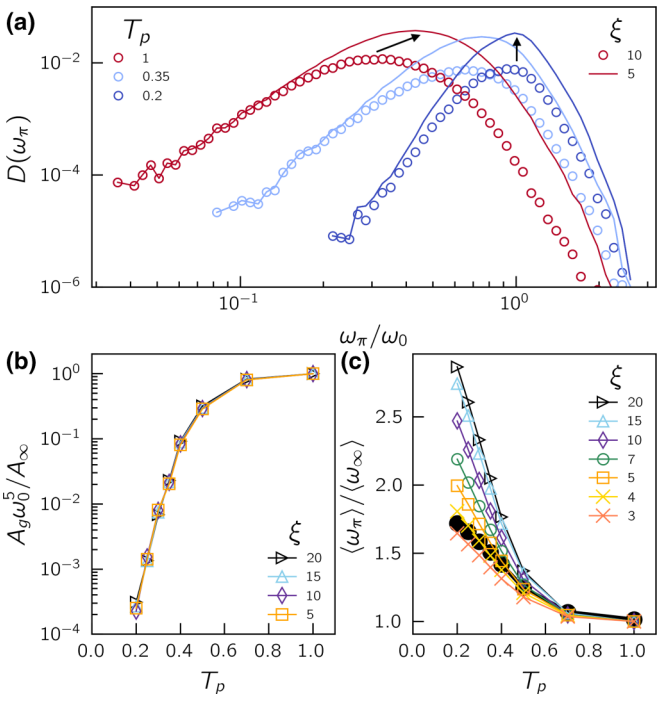

FIG. 9. (a) Comparison between the PHM vDOS extracted with $\xi = 10$ (empty circles) and $\xi = 5$ (solid lines) for different parent temperatures. (b) The prefactors A_g plotted vs the parent temperature T_p for various ξ. (c) The normalized characteristic frequency $\langle\omega_\pi\rangle/\langle\omega_\infty\rangle$ of quasilocalized modes for various ξ. Filled black circles are the normalized characteristic frequency of dipole responses taken from Ref. [45].

previously, we find the same qualitative behavior in two and three dimensions. Below T_{onset}, A_g drops by more than three orders of magnitude between the high-temperature plateau and the lowest temperature accessible by SWAP Monte Carlo, such as found in Ref. [25]. Moreover, the suppression of modes is postponed to slightly lower temperature in 2D compared to 3D solids.

As discussed extensively in Refs. [25,40], A_g is of units of an inverse frequency to the fifth power. Accordingly, a drop in A_g as a function of T_p is not necessarily caused by a decrease in the number density of QLEs populating the ω^4 scaling, but could be attributed to an overall mode stiffening. As such, we first need to quantify the characteristic frequency $\langle\omega_\pi\rangle$ of QLEs. In Fig. 10(b) we plot $\langle\omega_\pi\rangle$ normalized by the high parent temperature plateau $\langle\omega_\infty\rangle$ as a function of T_p. We find a stiffening of about a factor of two for both our 2D and 3D glasses. Consistent with the variability of A_g, the stiffening is weaker for 2D solids (about 25%–30%). This result is consistent with what has been found using the statistics of dipole responses [45]. One should, however, keep in mind that, strictly speaking, QLE's typical frequency $\langle\omega_\pi\rangle$ in two dimensions features a logarithmic dependence on system size L [20,40,51]. Here we have kept L fixed and consider the relative variability.

We now can compute the QLEs density as $\mathcal{N} = A_g\langle\omega_\pi\rangle^5$ and plot it against the inverse parent temperature $1/T_p$; see Fig. 10(c). As seen for A_g, $\mathcal{N}$ plateaus at high T_p but shows a weaker decrease with a drop of about two to three orders of magnitude when decreasing T_p. In both two and three dimensions, we observe an Arrhenius behavior where the QLEs depletion follows $\mathcal{N} \sim e^{-E_{qlm}/k_B T_p}$, with E_{qlm} a formation energy such as that found in Ref. [25].

Finally, we report in Fig. 10(d) the core size ξ_π as a function of T_p. For hyperquenched glasses (high T_p), the core size is about five to six particle diameters. This result is consistent with the typical coarse graining length scale used to quantitatively parametrized mesoscale elasto-plastic models

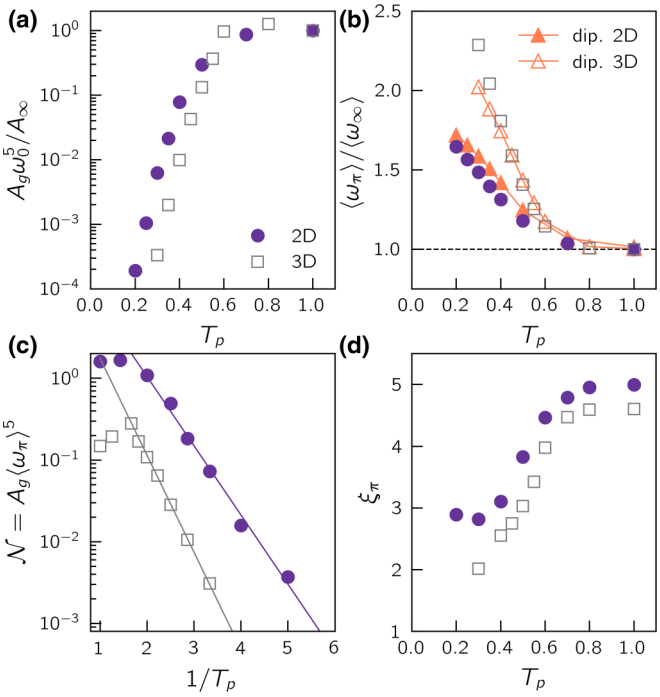

FIG. 10. (a) The prefactors A_g plotted vs the parent temperature T_p for both 2D and 3D glasses with $\xi = 5$. A_g is normalized by the high-temperature value $A_\infty = A_g(T_p = 1)$. (b) The normalized characteristic frequency $\langle\omega_\pi\rangle/\langle\omega_\infty\rangle$ of quasilocalized modes for $\xi = 3$. The orange data represent the characteristic frequency scale of dipole responses, taken from Ref. [45]. (c) The density $\mathcal{N}$ of QLEs, plotted as a function of $1/T_p$. Solid lines are linear regressions. (d) Core size ξ_π vs T_p.

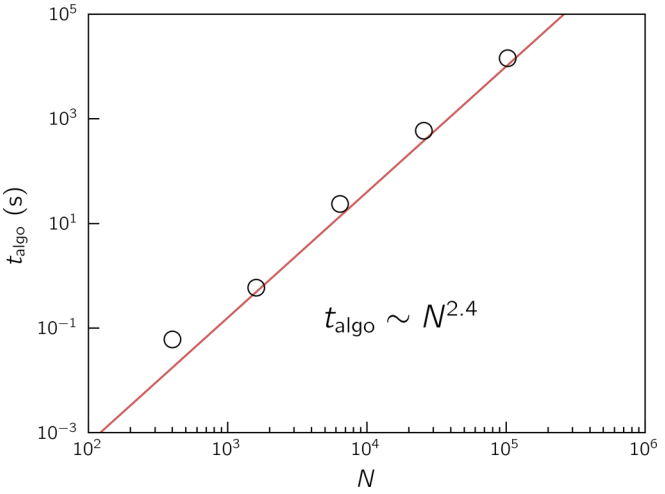

FIG. 11. Average time t_{algo} to build a catalog of QLEs in a glass composed of N particles with a block length $\xi = 20$. The solid line indicates the scaling $t_{algo} \sim N^{2.4}$.

from microscopic simulations [55,56]. We observe a factor two decrease of ξ_π when lowering T_p. This result is consistent with Ref. [25], where authors argued that the core size and the characteristic frequency scale are inversely proportional $\langle\omega_\pi\rangle \sim 1/\omega_\pi$. Accordingly, we find a slightly weaker decrease of ξ_π vs T_p in 2D compared with 3D glasses.

V. DISCUSSION AND CONCLUSION

In this paper we have presented a novel and efficient algorithm to detect the field of soft glassy excitations in structural glasses. Utilizing dipole forces as local probes, we have shown that one can construct the map of soft excitations in both two and three dimensions. We have highlighted that our detection algorithm suffers from a "halo" effect (see Sec. II C) created by the softest excitations present in the system: Once a mode with vanishing frequency exists in a given system, the minimization of the cost function $\mathcal{C}(z)$ will only converge to the same low-frequency solution. In other words, extremely soft modes result in cost functions $\mathcal{C}(z)$ featuring a single basin, which corresponds to the soft mode.

To circumvent this issue, we have put forward an easy biasing procedure where soft modes in the system are being stiffen by harmonic springs. This enables us to find soft excitations even for a system driven towards a plastic instability, during which the frequency of the destabilizing mode vanishes. We have benchmarked our algorithm with the harmonic spectrum of 3D glasses and have explored the influence of the algorithm parameters as well as the nonlinear cost function used. We have demonstrated that one can recover the correct asymptotic low-frequency nonphononic tail.

Using our algorithm, we have extracted the complete spectrum of localized soft excitations in 2D solids featuring a wide range of mechanical stability (generated using SWAP Monte Carlo). We have confirmed that the low-frequency limit of nonphononic excitations follows $D(\omega) = A_g\omega^4$, supporting recent claims [51,52]. Finally, we have reported how the dimensionless prefactor $A_g\omega_0^5$ and the characteristic mode frequency $\langle\omega_\pi\rangle$ change with thermal annealing. The same qualitative behavior is seen between 2D and 3D solids. We find a drop in the number density of QLEs $\mathcal{N} = A_g\langle\omega_\pi\rangle^5$ of about two to three orders of magnitude, a mode stiffening $\langle\omega_\pi\rangle$ of a factor two, and a factor two decrease of the core size ξ_π. This result confirms the previously established relation $\langle\omega_\pi\rangle \sim c_s/\xi_\pi$ between the QLE's characteristic frequency and the glassy length scale. Moreover, a 25%–30% weaker stiffening is observed in 2D glasses compared with their 3D counterpart. One could be tempted to draw an analogy between a stronger elastic stiffening mechanism in three dimensions, and the possible occurrence of a finite-temperature random first-order transition, which is likely to be absent in two dimensions [57].

This work opens avenues to understand elastic heterogeneities in amorphous solids. In particular, one can use nonlinear modes to access information on distributions of activation barriers, strain distances to instability [38], and tensorial information such that the softest shear direction. With our method, one will be able to monitor how these distributions change upon aging or mechanical deformation.

Furthermore, compared to modes built solely on the Hessian, cubic modes have the advantage to offer better core direction to move towards the nearby saddle. Thus, one could harvest the field of cubic modes to efficiently explore the potential energy landscape of a glass and improve existing methods such as saddle point sampling [18].

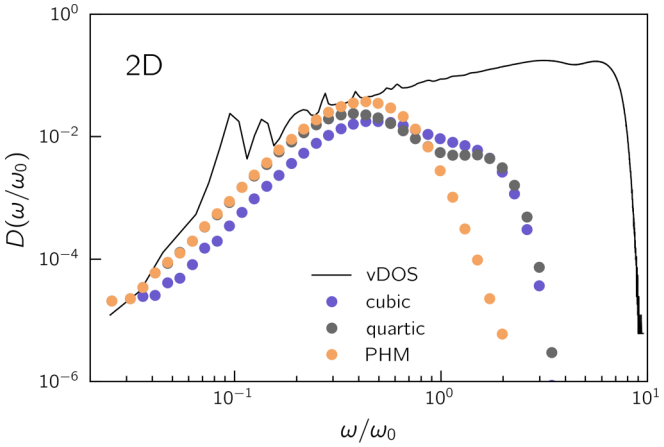

FIG. 12. Comparison between the 2D harmonic vDOS (solid black line) and the PHM spectra obtained from different cost functions: Cubic (purple), quartic (gray), and PHM (orange). The ensemble employed corresponds to poorly annealed glasses prepared at $T_p = 1$ with $N = 4096$.

ACKNOWLEDGMENTS

D.R. acknowledges support from the European Union's Horizon 2020 research and innovation programme under the Marie Sklodowska-Curie Grant Agreement No. 101024057. E.L. acknowledges support from the Netherlands Organisation for Scientific Research (NWO) (Vidi Grant No. 680-47-554/3259).

APPENDIX A: GLASS FORMER

Results shown in the main text are for two types of glass formers, polydisperse soft spheres and a 50–50 binary mixture. In both models, particles interact via a modified r^{-10} inverse power-law potential. A detailed description of these models is provided in Ref. [47]. Using SWAP Monte Carlo (MC) [46], we generate 2D and 3D polydisperse glasses with various degrees of stability. The later is controlled by the parent temperature T_p of the equilibrium states from which our glasses were instantaneously quenched. The binary mixture is quenched at a finite rate using conventional molecular dynamics. For both two and three dimensions, the onset temperature marking the rise of the shear modulus and viscous slowing down is $T_{onset} = 0.6$. All simulations are performed in the NVT ensemble with number density $N/V = 0.65$ (2D) and 0.58 (3D). Finally, we quench our configurations to zero temperature via an energy minimization using the conjugate gradient algorithm. All quantities in this paper are reported in dimensionless microscopic units: Lengths are rescaled by $a_0 = (V/N)^{1/d}$, frequencies by $\omega_0 = \sqrt{\mu_\infty/\rho}/a_0$, where μ_∞ is the plateau shear modulus of the high-parent temperature glasses. In order to convert our reduced units into conventional simulation units, we provide the high-temperature shear modulus plateau $\mu_\infty \simeq 10.35$ (2D) and $\mu_\infty \simeq 9.22$ (3D).

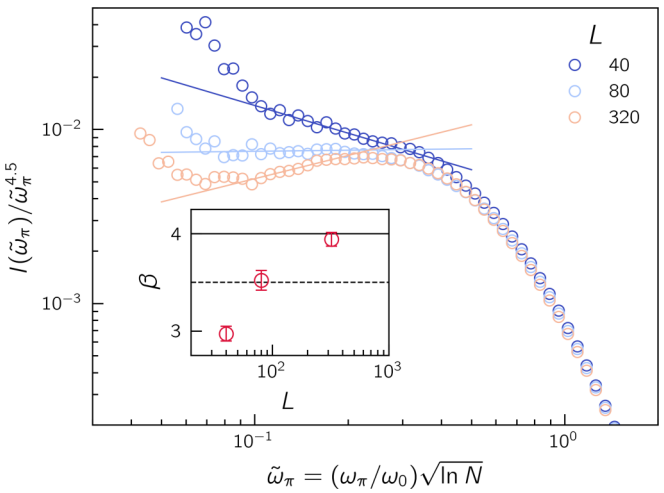

FIG. 13. Normalized cumulative distribution of the nonphonic vDOS for $\xi = 20$ and different system sizes. Frequencies are scales by $\sqrt{\ln N}$ to account for the log-correction present in 2D solids [51]. Solid lines are linear regressions, and the inset shows the corresponding exponents for the asymptotic scaling of the vDOS $D(\omega) \sim \omega^\beta$. Solid and dashed black lines indicate $\beta = 4$ and $\beta = 3.5$, respectively.

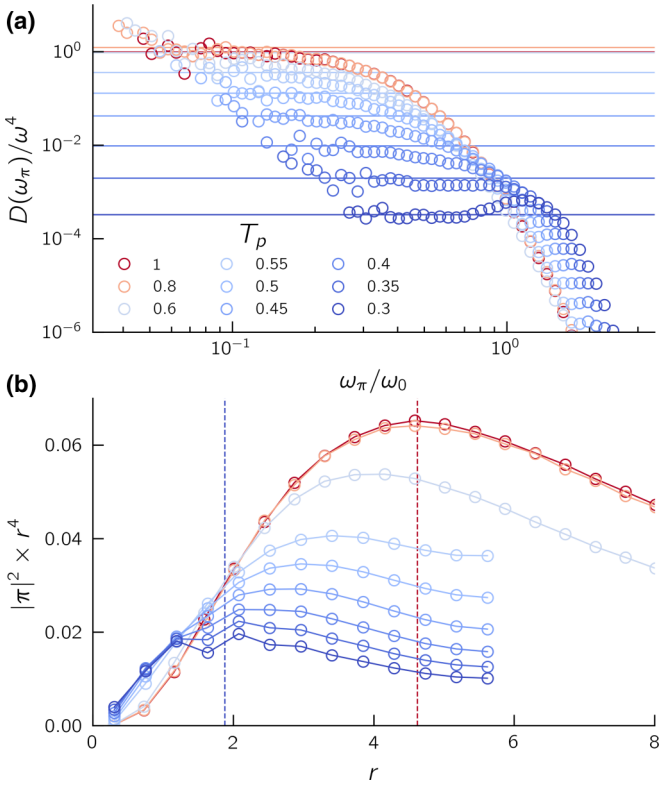

FIG. 14. (a) Rescaled PHM vDOS for various parent temperature T_p with $\xi = 5$. The horizontal lines indicate A_g. (b) Rescaled square of the mode amplitude decay $|\pi|^2$ by r^4. Vertical dashed lines indicate the reduced core size ξ_π when decreasing T_p.

APPENDIX B: ALGORITHM COMPLEXITY

We have checked for the complexity of our algorithm by computing the average time t_{algo} to build a catalog in a glass composed of N particles with $\xi = 20$; see Fig. 11. We find that t_{algo} scales with $N^{2.4}$. This result is explained by the combination of the trivial linear scaling of the number of

modes in the catalog with a fixed ξ and the additional linear scaling due to the complexity of solving linear equations for each mode. Finally, the "halo" effect is slightly pronounced in larger systems with the more likely presence of very low-frequency modes and the scaling $\xi_H \sim 1/\omega_\pi$. As a result, one needs more often to repeat step 4 of our algorithm.

APPENDIX C: COMPARISON OF DIFFERENT COST FUNCTIONS IN TWO DIMENSIONS

In Fig. 12 we provide the same data as in Fig. 5(c) but for 2D solids. We compare the harmonic vDOS with the spectra of nonlinear modes obtained with different cost functions. We find similar behavior as for 3D solids. In the low-frequency regime, quartic and PHM excitations have the lowest energy and converge to harmonic modes. At high frequencies, we observe a second peak for cubic and quartic modes, which is absent in the PHM spectra.

APPENDIX D: FINITE-SIZE EFFECT: 2D NONPHONONIC SPECTRUM

As shown in the main text and discussed in Refs. [48–52], small hyperquenched glasses (high T_p) in two dimensions exhibit a different asymptotic scaling for the nonphonic vDOS, namely, $D(\omega) \sim \omega^\beta$ with $\beta < 4$. Here we apply our algorithm to compute the cumulative distribution $I(\omega)$ in poorly annealed IPL binary mixtures with different system sizes; see Fig. 13. For a system composed of a few thousand of particles, $I(\omega)$ shows a low-frequency plateau when rescaled by $\omega^{4.5}$ (i.e., $\beta = 3.5$). In contrast for the largest system $N = 102\,400$ ($L = 320$), we find that the rescaled cumulative distribution dips and scales as $\sim\omega^5$, which translates to $\beta = 4$ such as found in mildly annealed 2D glasses (cf. Fig. 8).

APPENDIX E: NONPHONONIC SPECTRUM OF 3D STRUCTURAL GLASSES

Here we provide additional data for 3D glasses used to extract the nonphononic prefactor A_g, the mode frequency $\langle\omega_\pi\rangle$, and the core size ξ_π. In Fig. 14(a) we plot the rescaled PHM vDOS to highlight the range of A_g (low-frequency plateau) as a function of the parent temperature T_p. Consistent with Ref. [25], we observe a drop of three orders of magnitude in A_g from hyperquenched glasses to very stable glasses obtained via SWAP Monte Carlo.

Extracting the lowest mode of each glassy sample, we compute the the average of the square of the mode amplitude decay $|\pi|^2$. In Fig. 14(b) we plot the rescaled mode decay by its r^{-4} asymptotic scaling. The peak in $r^4|\pi|^2$ allows us to extract an estimate for ξ_π. We find a factor two decrease of the core size of soft glassy of excitations, consistent with the work done in Ref. [25] and with the factor two increase of the typical mode frequency $\langle\omega_\pi\rangle$.

[1] A. Argon and M. Salama, The mechanism of fracture in glassy materials capable of some inelastic deformation, Mater. Sci. Eng. **23**, 219 (1976).

[2] F. Spaepen, A microscopic mechanism for steady state inhomogeneous flow in metallic glasses, Acta Metall. **25**, 407 (1977).

[3] D. Richard, M. Ozawa, S. Patinet, E. Stanifer, B. Shang, S.A. Ridout, B. Xu, G. Zhang, P. K. Morse, J. L. Barrat *et al.*, Predicting plasticity in disordered solids from structural indicators, Phys. Rev. Mater. **4**, 113609 (2020).

[4] D. Coslovich and G. Pastore, Understanding fragility in supercooled Lennard-Jones mixtures. I. Locally preferred structures, J. Chem. Phys. **127**, 124504 (2007).

[5] A. Malins, S. R. Williams, J. Eggers, and C. P. Royall, Identification of structure in condensed matter with the topological cluster classification, J. Chem. Phys. **139**, 234506 (2013).

[6] H. Tong and H. Tanaka, Revealing hidden structural order controlling both fast and slow glassy dynamics in supercooled liquids, Phys. Rev. X **8**, 011041 (2018).

[7] P. Ronhovde, S. Chakrabarty, D. Hu, M. Sahu, K. Sahu, K. Kelton, N. Mauro, and Z. Nussinov, Detecting hidden spatial and spatio-temporal structures in glasses and complex physical systems by multiresolution network clustering, Eur. Phys. J. E **34**, 105 (2011).

[8] E. D. Cubuk, S. S. Schoenholz, J. M. Rieser, B. D. Malone, J. Rottler, D. J. Durian, E. Kaxiras, and A. J. Liu, Identifying structural flow defects in disordered solids using machine-learning methods, Phys. Rev. Lett. **114**, 108001 (2015).

[9] E. Boattini, S. Marín-Aguilar, S. Mitra, G. Foffi, F. Smallenburg, and L. Filion, Autonomously revealing hidden local structures in supercooled liquids, Nat. Commun. **11**, 5479 (2020).

[10] J. Paret, R. L. Jack, and D. Coslovich, Assessing the structural heterogeneity of supercooled liquids through community inference, J. Chem. Phys. **152**, 144502 (2020).

[11] V. Bapst, T. Keck, A. Grabska-Barwińska, C. Donner, E. D. Cubuk, S. S. Schoenholz, A. Obika, A. W. Nelson, T. Back, D. Hassabis *et al.*, Unveiling the predictive power of static structure in glassy systems, Nat. Phys. **16**, 448 (2020).

[12] Z. Fan and E. Ma, Predicting orientation-dependent plastic susceptibility from static structure in amorphous solids via deep learning, Nat. Commun. **12**, 1506 (2021).

[13] G. Jung, G. Biroli, and L. Berthier, Predicting dynamic heterogeneity in glass-forming liquids by physics-inspired machine learning, Phys. Rev. Lett. **130**, 238202 (2023).

[14] A. Tanguy, B. Mantisi, and M. Tsamados, Vibrational modes as a predictor for plasticity in a model glass, EPL (Europhys. Lett.) **90**, 16004 (2010).

[15] M. L. Manning and A. J. Liu, Vibrational modes identify soft spots in a sheared disordered packing, Phys. Rev. Lett. **107**, 108302 (2011).

[16] M. Tsamados, A. Tanguy, C. Goldenberg, and J.-L. Barrat, Local elasticity map and plasticity in a model Lennard-Jones glass, Phys. Rev. E **80**, 026112 (2009).

[17] S. Patinet, D. Vandembroucq, and M. L. Falk, Connecting local yield stresses with plastic activity in amorphous solids, Phys. Rev. Lett. **117**, 045501 (2016).

[18] B. Xu, M. L. Falk, J. F. Li, and L. T. Kong, Predicting shear transformation events in metallic glasses, Phys. Rev. Lett. **120**, 125503 (2018).
[19] Z. Schwartzman-Nowik, E. Lerner, and E. Bouchbinder, Anisotropic structural predictor in glassy materials, Phys. Rev. E **99**, 060601(R) (2019).
[20] G. Kapteijns, E. Bouchbinder, and E. Lerner, Universal nonphononic density of states in 2D, 3D, and 4D glasses, Phys. Rev. Lett. **121**, 055501 (2018).
[21] E. Lerner, G. Düring, and E. Bouchbinder, Statistics and properties of low-frequency vibrational modes in structural glasses, Phys. Rev. Lett. **117**, 035501 (2016).
[22] H. Mizuno, H. Shiba, and A. Ikeda, Continuum limit of the vibrational properties of amorphous solids, Proc. Natl. Acad. Sci. USA **114**, E9767 (2017).
[23] L. Angelani, M. Paoluzzi, G. Parisi, and G. Ruocco, Probing the non-Debye low-frequency excitations in glasses through random pinning, Proc. Natl. Acad. Sci. USA **115**, 8700 (2018).
[24] L. Wang, A. Ninarello, P. Guan, L. Berthier, G. Szamel, and E. Flenner, Low-frequency vibrational modes of stable glasses, Nat. Commun. **10**, 26 (2019).
[25] C. Rainone, E. Bouchbinder, and E. Lerner, Pinching a glass reveals key properties of its soft spots, Proc. Natl. Acad. Sci. USA **117**, 5228 (2020).
[26] D. Richard, K. González-López, G. Kapteijns, R. Pater, T. Vaknin, E. Bouchbinder, and E. Lerner, Universality of the nonphononic vibrational spectrum across different classes of computer glasses, Phys. Rev. Lett. **125**, 085502 (2020).
[27] K. Shiraishi, Y. Hara, and H. Mizuno, Low-frequency vibrational states in ideal glasses with random pinning, Phys. Rev. E **106**, 054611 (2022).
[28] C. Maloney and A. Lemaitre, Universal breakdown of elasticity at the onset of material failure, Phys. Rev. Lett. **93**, 195501 (2004).
[29] H. G. E. Hentschel, S. Karmakar, E. Lerner, and I. Procaccia, Do athermal amorphous solids exist? Phys. Rev. E **83**, 061101 (2011).
[30] G. Kapteijns, D. Richard, E. Bouchbinder, and E. Lerner, Elastic moduli fluctuations predict wave attenuation rates in glasses, J. Chem. Phys. **154**, 081101 (2021).
[31] L. Wang, L. Berthier, E. Flenner, P. Guan, and G. Szamel, Sound attenuation in stable glasses, Soft Matter **15**, 7018 (2019).
[32] S. Mahajan and M. P. Ciamarra, Unifying description of the vibrational anomalies of amorphous materials, Phys. Rev. Lett. **127**, 215504 (2021).
[33] D. Richard, E. Lerner, and E. Bouchbinder, Brittle-to-ductile transitions in glasses: Roles of soft defects and loading geometry, MRS Bull. **46**, 902 (2021).
[34] E. Bouchbinder and E. Lerner, Universal disorder-induced broadening of phonon bands: From disordered lattices to glasses, New J. Phys. **20**, 073022 (2018).
[35] D. Richard, G. Kapteijns, J. A. Giannini, M. L. Manning, and E. Lerner, Simple and broadly applicable definition of shear transformation zones, Phys. Rev. Lett. **126**, 015501 (2021).
[36] L. Gartner and E. Lerner, Nonlinear plastic modes in disordered solids, Phys. Rev. E **93**, 011001(R) (2016).
[37] L. Gartner and E. Lerner, Nonlinear modes disentangle glassy and goldstone modes in structural glasses, SciPost Phys. **1**, 016 (2016).
[38] G. Kapteijns, D. Richard, and E. Lerner, Nonlinear quasilocalized excitations in glasses: True representatives of soft spots, Phys. Rev. E **101**, 032130 (2020).
[39] S. Wijtmans and M. L. Manning, Disentangling defects and sound modes in disordered solids, Soft Matter **13**, 5649 (2017).
[40] E. Lerner and E. Bouchbinder, A characteristic energy scale in glasses, J. Chem. Phys. **148**, 214502 (2018).
[41] E. Lerner and E. Bouchbinder, Low-energy quasilocalized excitations in structural glasses, J. Chem. Phys. **155**, 200901 (2021).
[42] E. Lerner and E. Bouchbinder, Boson-peak vibrational modes in glasses feature hybridized phononic and quasilocalized excitations, J. Chem. Phys. **158**, 194503 (2023).
[43] M. Lerbinger, A. Barbot, D. Vandembroucq, and S. Patinet, Relevance of shear transformations in the relaxation of supercooled liquids, Phys. Rev. Lett. **129**, 195501 (2022).
[44] A. Widmer-Cooper, H. Perry, P. Harrowell, and D. R. Reichman, Irreversible reorganization in a supercooled liquid originates from localized soft modes, Nat. Phys. **4**, 711 (2008).
[45] C. Rainone, E. Bouchbinder, and E. Lerner, Statistical mechanics of local force dipole responses in computer glasses, J. Chem. Phys. **152**, 194503 (2020).
[46] A. Ninarello, L. Berthier, and D. Coslovich, Models and algorithms for the next generation of glass transition studies, Phys. Rev. X **7**, 021039 (2017).
[47] E. Lerner, Mechanical properties of simple computer glasses, J. Non-Cryst. Solids **522**, 119570 (2019).
[48] L. Wang, G. Szamel, and E. Flenner, Low-frequency excess vibrational modes in two-dimensional glasses, Phys. Rev. Lett. **127**, 248001 (2021).
[49] L. Wang, G. Szamel, and E. Flenner, Erratum: Low-frequency excess vibrational modes in two-dimensional glasses [Phys. Rev. Lett. **127**, 248001 (2021)], Phys. Rev. Lett. **129**, 019901(E) (2022).
[50] L. Wang, G. Szamel, and E. Flenner, Scaling of the nonphononic spectrum of two-dimensional glasses, J. Chem. Phys. **158**, 126101 (2023).
[51] E. Lerner and E. Bouchbinder, Nonphononic spectrum of two-dimensional structural glasses, J. Chem. Phys. **157**, 166101 (2022).
[52] K. Shiraishi, H. Mizuno, and A. Ikeda, Non-phononic density of states of two-dimensional glasses revealed by random pinning, J. Chem. Phys. **158**, 174502 (2023).
[53] E. Lerner, Finite-size effects in the nonphononic density of states in computer glasses, Phys. Rev. E **101**, 032120 (2020).
[54] J. A. Giannini, D. Richard, M. L. Manning, and E. Lerner, Bond-space operator disentangles quasilocalized and phononic modes in structural glasses, Phys. Rev. E **104**, 044905 (2021).
[55] D. F. Castellanos, S. Roux, and S. Patinet, Insights from the quantitative calibration of an elasto-plastic model from a Lennard-Jones atomic glass, C. R. Phys. **22**, 135 (2021).
[56] C. Liu, S. Dutta, P. Chaudhuri, and K. Martens, Elastoplastic approach based on microscopic insights for the steady state and transient dynamics of sheared disordered solids, Phys. Rev. Lett. **126**, 138005 (2021).
[57] B. Guiselin, L. Berthier, and G. Tarjus, Statistical mechanics of coupled supercooled liquids in finite dimensions, SciPost Phys. **12**, 091 (2022).